FIGURES AND LEGENDS

Figure 1

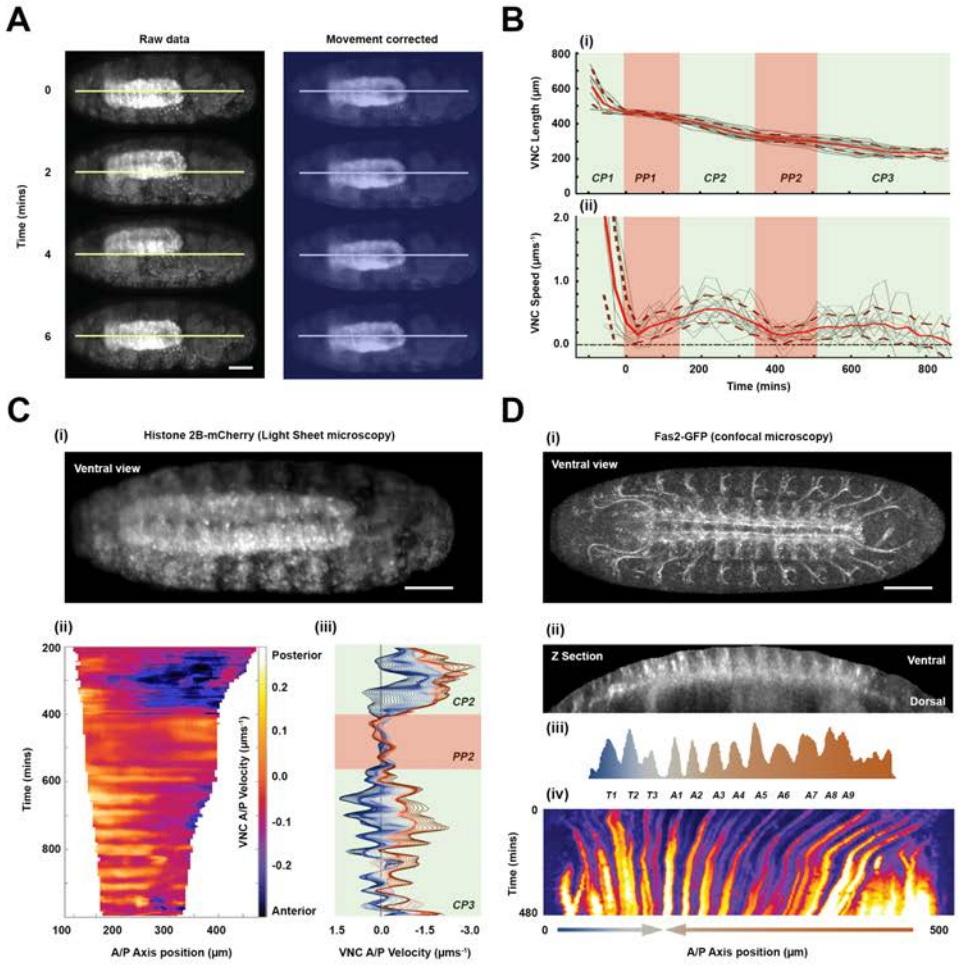

Figure 1: Dynamics of VNC condensation

A) Snapshots at 2-minute intervals from a time lapse **(Movie S3)** recorded by multi-view light-sheet imaging of a live Histone 2Av-mCherry embryo (ventral view – late stage 17). mCherry labeling marks all nuclei and was used to correct the embryo twitching (see Experimental Procedures); raw data is shown on the left and "detwitched" images (blue masked) on the right. In all images, anterior is to the left and posterior to the right. Lines indicate the ventral midline. Scale bar 50 µm. **B)** Quantification of VNC length (**i**) and condensation speed (**ii**) as function of time. Condensation (CP1, CP2 and CP3) and pause (PP1 and PP2) phases are masked in pale green and red respectively. As a convention for this and all subsequent figures (unless stated otherwise), t=0 corresponds to the onset of the VNC pause phase (PP1), at the end of germ band retraction. Means (solid) and SD (dashed) are represented by red lines. Gray lines represent individual embryos (n=11 embryos). **C)** Condensation velocity spatiotemporal dynamics. (**i**) Snapshot of a live Histone 2Av-mCherry embryo monitored by light-sheet imaging at stage 16. Scale bar 50 µm. (**ii**) Velocity kymograph derived from PIV analysis (Experimental Procedures) along the VNC. For this and all subsequent figures, position=0 along the AP axis corresponds to the hinge between the brain lobes and the VNC proper. Time axis (top to bottom) was defined as in **(B)**. Color-coded positive (posterior-ward - white/yellow) and negative (anterior-ward - black/blue) values of velocity (neutral - red). **(iii)** Representation of velocity profiles along the whole condensation process (CP2, PP2 and CP3), with 5-minute resolution, for all points along the AP axis from the most anterior (darkest blue) to the most posterior (darkest red lines) VNC positions. **D)** Kymograph along the VNC length from a live embryo expressing Fas2-GFP. (**i**) Ventral view from a confocal microscopy acquisition **(Movie S4)**, at stage 16. Scale bar 50 µm. (**ii**) Stage 16 embryonic VNC, re-sliced over the Z-axis. (**iii**) Fluorescence intensity peaks mark individual segments landmarks (color coded as in **(C)**). Time and AP axis positions are as in **(B)** and **(C)**. (**iv**) Kymograph of condensation, with arrows denoting condensation direction.

Figure 2

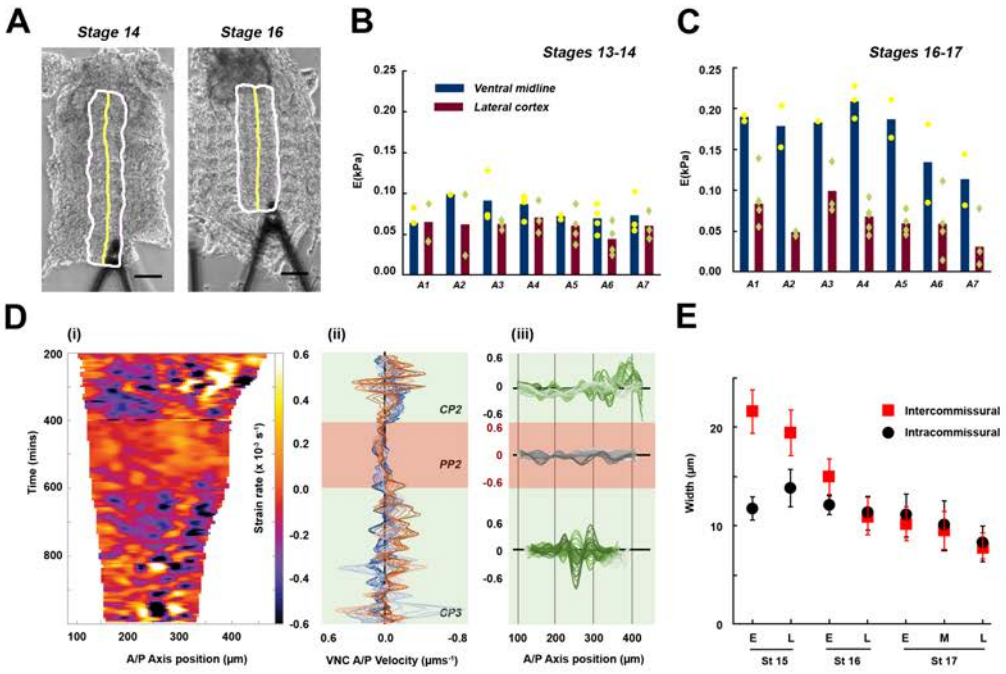

Figure 2: Characterization of the VNC material properties and local dynamics along its condensation

A) Representative images of flat dissected embryos in stages 14 and stages 16, respectively. VNC perimeter (white line) and midline (yellow line) are highlighted, with the AFM cantilever head shown. Anterior is to the top. Scale bar 50 µm. **B)** Measured tissue stiffness (E) for dissected VNC at early stages (13-14). Bars denote mean values at each abdominal segment A1 to A7. Mean tissue stiffness was measured at the midline (blue) and at lateral positions of the cortex (red). Dots and diamonds correspond to individual measurements. **C)** as **(B)** but for later, stage 16-17, samples. **D)** (**i**) Kymograph

of VNC strain rates, from data in **Figure 1C** (see Experimental Procedures). (**ii**) Representation of strain rates profiles during condensation (CP2, PP2 and CP3), with 5-minute resolution, from the most anterior (darkest blue line) to the most posterior (darkest red line) VNC positions. (**iii**) Distribution of strains in VNC along the AP- axis for all time points (earliest light to latest dark lines) during the phases CP2 (green), PP2 (gray) and CP3 (green). **E)** Average size (and SD) of intra- and inter-commissural domains from early (E) and late (L) stage 15, early (E) and late (L) stage 16 and early (E), middle (M) and late (L) stage 17 embryos as the VNC condenses. Data was collected from 7-10 measurements per time point from two embryos.

Figure 3

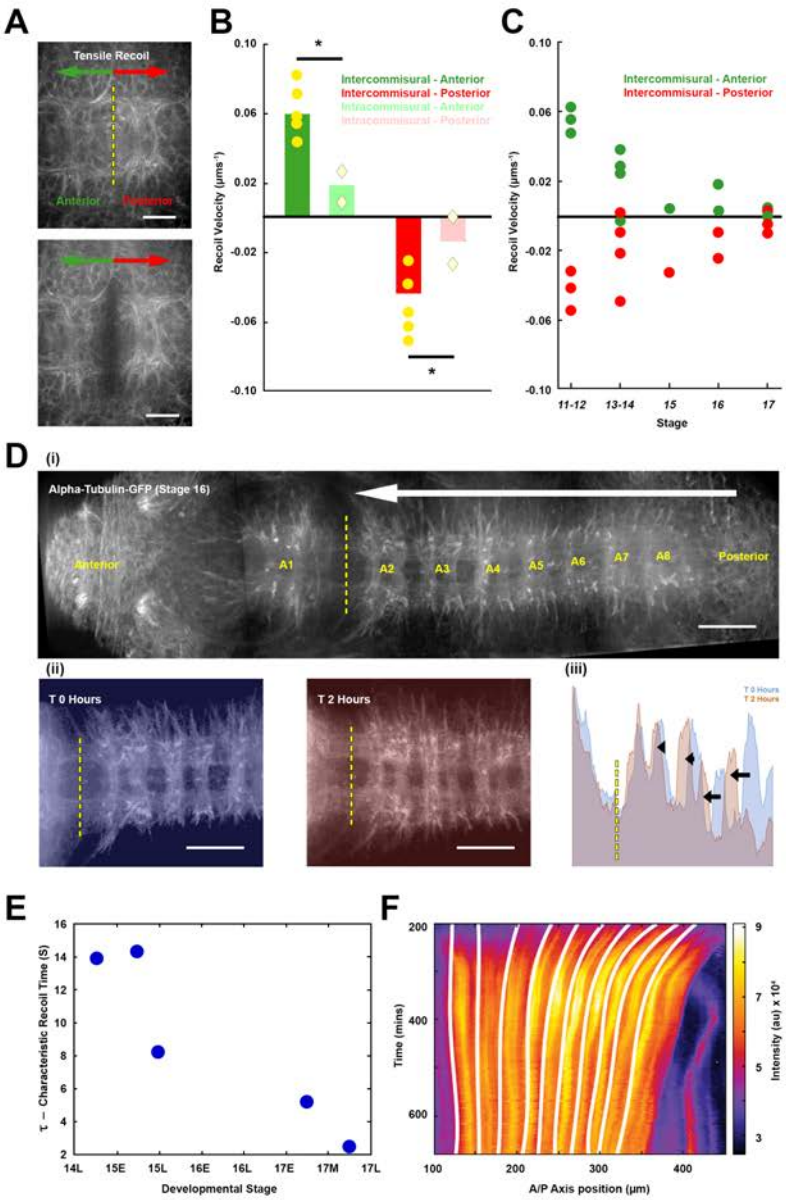

Figure 3: VNC response to laser microsurgery during condensation and tissue tension

A) Representative images of stage 14 embryos, expressing alpha Tubulin-GFP, before (top) and after (bottom) laser ablation. The yellow dashed line highlights the position of the laser cut (intercommissural), while green (anterior) and red (posterior) arrows indicate

tensile recoil directionality **(Movie S5)**. Scale bar 10 µm. **B)** Tensile recoil velocity after ablation at intercommissural (dark) and intracommissural (pale) domains, on stage 14 embryos. Bars represent mean recoil velocity of anteriorly (green) and posteriorly (red) retracting tissue. Individual measurements are denoted by yellow dots (intercommissural) and diamonds (intracommissural). * $p < 0.05$. **C)** Recoil velocity of anteriorly (green) and posteriorly (red) retracting domains after VNC ablation at different stages of embryonic development (n=12 embryos). **D)** (**i**) Tiled image of a stage 16 embryo expressing alpha Tubulin-GFP after laser cutting the intercommissural domain between the abdominal segments A1 and A2. The white arrow marks the direction of tissue condensation. The anterior and posterior limits of the VNC and the different abdominal segments (A1 to A8) are indicated (yellow). (**ii**) Snapshots, immediately post-ablation (masked blue), and 2 hours later (masked red), from **Movie S6**. Scale bar 20 µm. (**iii**) Superimposed fluorescence intensity profiles of both time points. Black arrows indicate the magnitude of the anterior-ward displacement of individual segmental landmarks over the analyzed period. **E)** Characteristic recoil time τ at different embryonic stages computed from the rate of recoil after laser ablation at the intercommissural domain. **F)** Kymograph of the VNC during condensation (Fas2-GFP expressing embryo). White curves correspond to fourth order polynomial fitting of the points of maximum compression as deduced from the viscoelastic FE model of the VNC (Experimental Procedures). (See also **Figure S4D** and **Movie S7**).

Figure 4

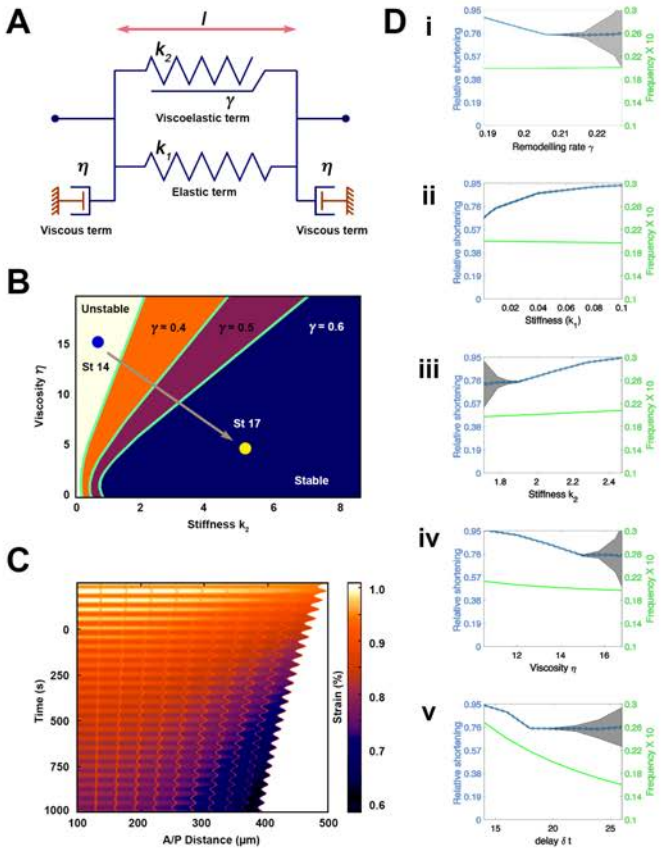

Figure 4: Rheological model of VNC condensation

A) Scheme of one-dimensional rheological model. A viscoelastic term with variable rest-length l has stiffness k_2 and remodeling rate γ (see Eq. (1) in Results). The VNC is taken to have an elastic component in parallel, with stiffness k_1. The model also includes viscous contact to the external environment, denoted by η. **B)** Phase diagram in the parameter space k_2 - η, showing that reduction of η and increase of k_2 stabilizes the oscillatory behavior. Points St 14 and St 17 represent material values and transition from early to later stages of VNC development, with a stabilizing effect. **C)** Kymograph of numerical simulation showing the oscillatory behavior of strains as a function of time. Simulations with other parameter values showing unstable responses are shown in **Figure S5**. **D)**

Sensitivity of VNC shortening and oscillatory frequencies to main model parameters on. (**i**) Remodelling rate, γ. (**ii**) Stiffness, k_1. (**iii**) Stiffness, k_2. (**iv**) Viscosity, η. (**v**) Time delay, δt. Shortening is measured as the relative final length, l_{final} / l_0. The dotted blue line indicates the initial amplitude of the oscillations for the model reference parameters (γ, k_1, k_2, η, δt) = (0.2, 0.01, 1.9, 15, 20), while the gray area represents the final amplitude for the analyzed value of the parameter indicated on the horizontal axis. The green line indicates the oscillations frequency as a function of the parameter values. Frequency is measured in min^{-1} *10.

Figure 5

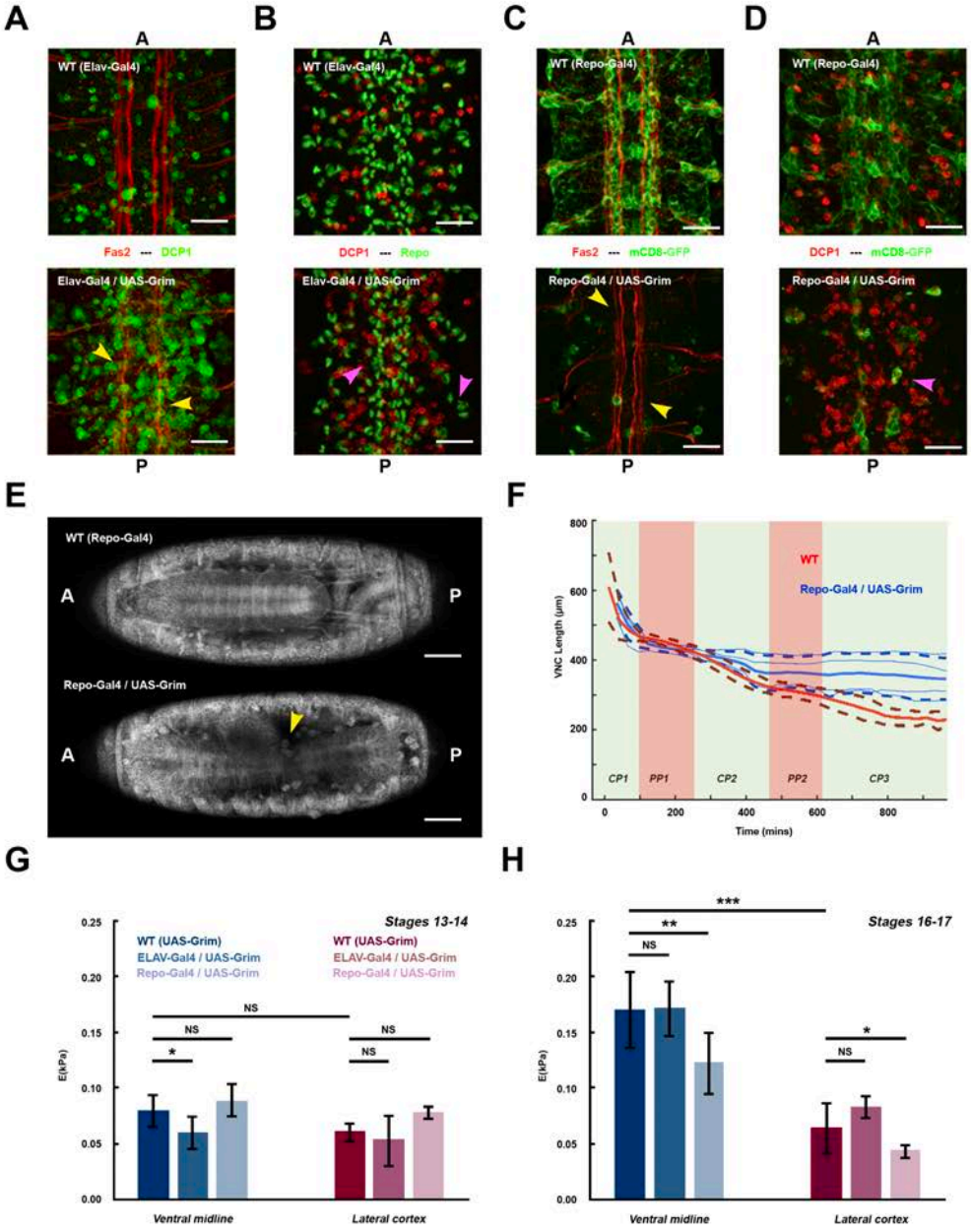

Figure 5: Both neurons and glia participate in the architectural organization of the VNC and its condensation

A) CNS Flat-preps of WT (top) and Elav-Gal4>UAS-Grim (bottom) embryos, at stage 16, immunostained for Fas2 (red) and Dcp1 (green). Yellow arrowheads point to the disrupted axonal network. **B)** Embryos of the same genotype as in **(A)**, immunostained for Dcp1 (red) and Repo (green). Pink arrowheads point to misplaced glia. **C)** CNS Flat-

preps of WT (top) and Repo-Gal4:UAS-mCD8-GFP>UAS-Grim (bottom) embryos, at stage 16, immunostained for Fas2 (red) and GFP (green). Yellow arrowheads point to the disrupted axonal network. **D)** Embryos of the same genotype as in **(C)**, immunostained for Dcp1 (red) and GFP (green). Pink arrowhead points to surviving glia. Scale bar 10 µm in **A-D**. **E)** Snapshots from time lapse recordings of WT (Top) and Repo-Gal4>UAS-Grim (bottom) embryos, in an alpha Tubulin-GFP background (ventral view –stage 17) **(Movie S8)**. Yellow arrowhead points to the VNC misshaped buckling. Scale bar 50 µm. AP axis orientation is indicated. **F)** Quantification of VNC length as a function of developmental time in WT (red, n=11) and Repo-Gal4>UAS-Grim (blue, n=4) embryos marked with *elav*:mCD8-GFP by confocal imaging. Solid and dashed lines show mean and SD values respectively. **G)** Tissue stiffness (E) measured by AFM for dissected VNCs at early stages (13-14), from WT, Elav-Gal4>UAS-Grim and Repo-Gal4>UAS-Grim embryos. Bars denote mean values at the ventral midline (blue) and at lateral cortex areas (red). *$p < 0.05$, **$p < 10^{-2}$ and ***$p < 10^{-3}$. **H)** As **(G)** but for later stage 16-17 embryos.

Figure 6

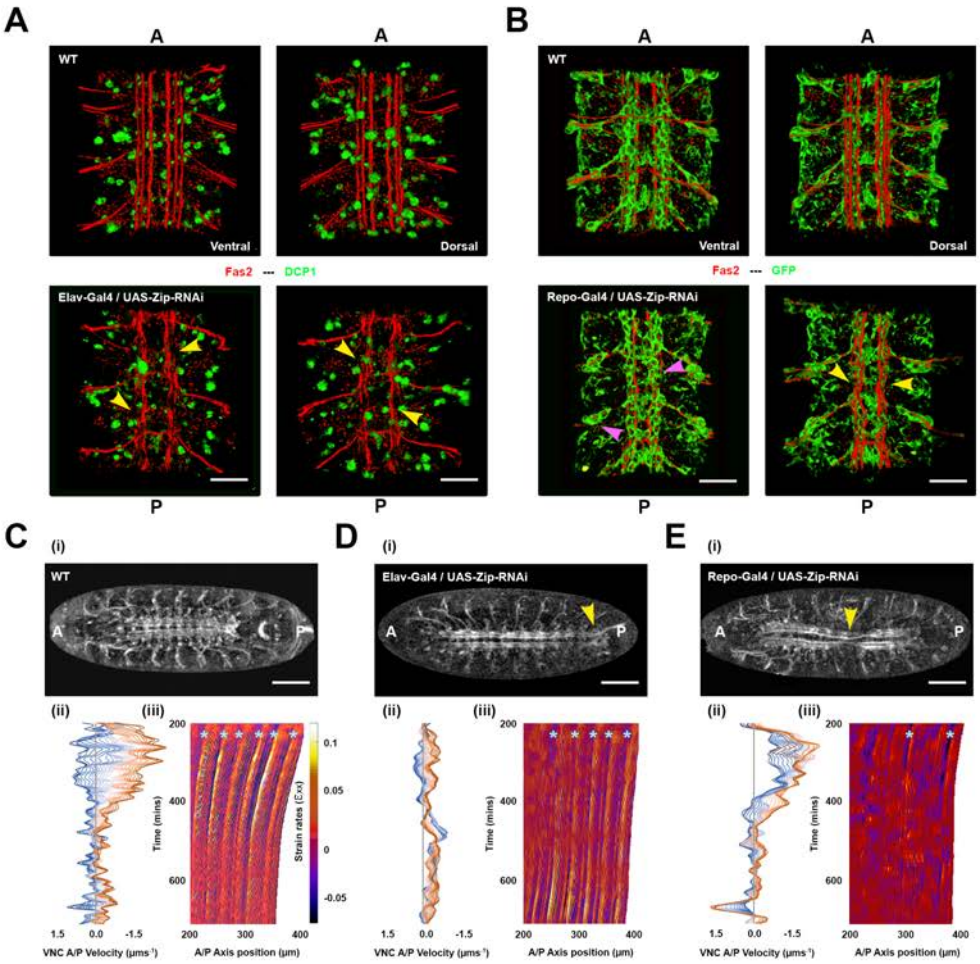

Figure 6: Active contractility in neurons and glia have distinct roles for VNC architecture and condensation.

A) Ventral and Dorsal 3D views of dissected, stage 16, WT (top) and Elav-Gal4>UAS-Zip-RNAi (bottom) embryos, immunostained for Fas2 (red) and Dcp1 (green). Yellow arrowheads point to the disrupted axonal network. **B)** Ventral and Dorsal 3D views, equivalent to (**A**), of stage 16, WT (top) and Repo-Gal4:UAS-mCD8-GFP>UAS-Zip-RNAi (bottom) embryos, immunostained for Fas2 (red) and GFP (green). Pink arrowheads point to misplaced glia. Yellow arrowheads point to the disrupted axonal

network. **A-B** Scale bar 10 µm. **C-E)** Condensation dynamics in control **(C)**, Elav-Gal4>UAS-Zip-RNAi **(D)** and Repo-Gal4>UAS-Zip-RNAi **(E)** embryos **(Movie S10)**. (**i**) Snapshots of live embryos, expressing Fas2-GFP, monitored by confocal imaging, at stage 17. Yellow arrowheads point to the posterior tip of the uncondensed VNC **(D)** and to the VNC misshaped buckling (**E**). Anterior is to the left. Scale bar 50 µm. (**ii**) Representation of velocity profiles during condensation along the AP axis, from the most anterior (darkest blue) to the most posterior (darkest red line) VNC positions (as in **Figure 1C**). (**iii**) Kymograph of strain rates along the VNC (as **Figure 2D**). Cyan marks point to strain oscillations, which are strongly diminished upon reduction of glia contractility.

Figure 7

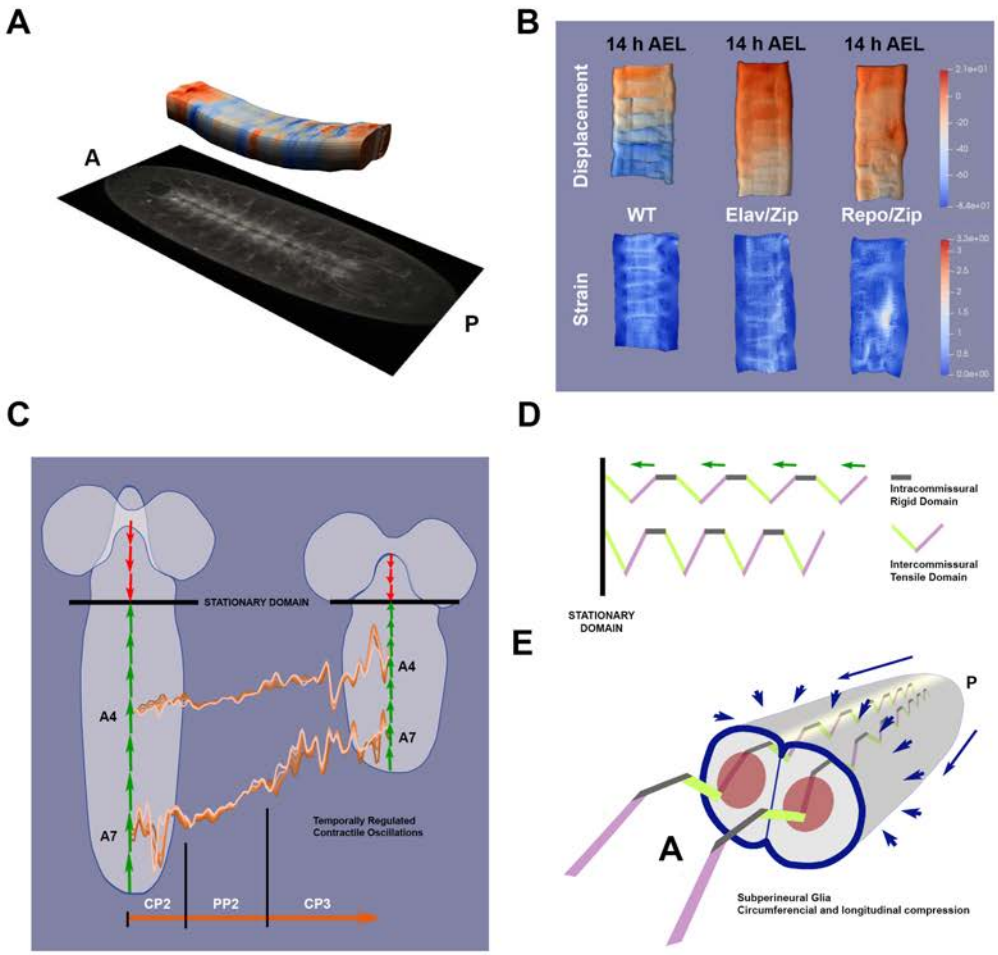

142

143 **Figure 7: Neurons and Glia cooperate to lead the oscillatory character of VNC**
144 **condensation**

145 **A)** Snapshot from the 3D representation **(Movie S11)** of the segmental 2D strain pattern
146 of the VNC during condensation, in WT animals. The actual 3D meshwork (top) is
147 aligned to the corresponding raw image (bottom). AP axis orientation is indicated. **B)**
148 Displacements and strains along the VNC, in WT embryos and in embryos with pan-
149 neural (Elav-Gal4>UAS-Zip-RNAi) or pan-glial (Repo-Gal4>UAS-Zip-RNAi) non

muscle Myosin II knockdown, at equivalent developmental times [14 hours after egg laying (AEL) at 29ºC]. **(**Snapshots from **Movie S12)**. **C)** Cartoon summarizing the VNC condensation oscillatory regime during the CP2 and CP3 stages (examples at the level of the abdominal segments A4 and A7, data from **Movie S3** – see **Figure 1C**), as well as pointing to the opposing displacements of the thoracic (red) and abdominal (green) segments towards the central stationary domain. **D)** Cartoon presenting the segmentally iterated intercommissural and intracommissural domains of the axonal network before (top) and after (bottom) condensation. Their mechanical properties (rigid or tensile) are shown. This representation depicts the first three abdominal segments actively contracting (green arrows) towards the thorax/abdomen stationary domain. **E)** Cartoon presenting in 3D the VNC internal segmentally iterated axonal network (described in **D**) surrounded by the glial shell (Subperineural Glia) with centripetal and longitudinal contractile capability (blue arrows). AP axis orientation is indicated.

REFERENCES

Amourda, C., and Saunders, T.E. (2017). Gene expression boundary scaling and organ size regulation in the Drosophila embryo. Dev Growth Differ *59*, 21-32.

Anava, S., Greenbaum, A., Ben Jacob, E., Hanein, Y., and Ayali, A. (2009). The regulative role of neurite mechanical tension in network development. Biophys J *96*, 1661-1670.

Baines, R.A., and Bate, M. (1998). Electrophysiological development of central neurons in the Drosophila embryo. J Neurosci *18*, 4673-4683.

Barriga, E.H., Franze, K., Charras, G., and Mayor, R. (2018). Tissue stiffening coordinates morphogenesis by triggering collective cell migration in vivo. Nature *554*, 523-527.

Beckervordersandforth, R.M., Rickert, C., Altenhein, B., and Technau, G.M. (2008). Subtypes of glial cells in the Drosophila embryonic ventral nerve cord as related to lineage and gene expression. Mech Dev *125*, 542-557.

Bertet, C., Sulak, L., and Lecuit, T. (2004). Myosin-dependent junction remodelling controls planar cell intercalation and axis elongation. Nature *429*, 667-671.

Boix-Fabres, J., Karkali, K., Martin-Blanco, E., and Rebollo, E. (2019). Automated Macro Approach to Remove Vitelline Membrane Autofluorescence in Drosophila Embryo 4D Movies. Methods Mol Biol *2040*, 155-175.

Bullmore, E., and Sporns, O. (2012). The economy of brain network organization. Nature reviews Neuroscience *13*, 336-349.

Bullock, T.H., and Horridge, G.A. (1965). Structure and function in the nervous systems of invertebrates (San Francisco: W. H. Freeman).

Buszczak, M., Paterno, S., Lighthouse, D., Bachman, J., Planck, J., Owen, S., Skora, A.D., Nystul, T.G., Ohlstein, B., Allen, A.*, et al.* (2007). The carnegie protein trap library: a versatile tool for Drosophila developmental studies. Genetics *175*, 1505-1531.

Cajal, S.R.y. (1899). Textura del Sistema Nervioso del Hombre y de los Vertebrados (Madrid, Spain: Nicolas Moya).

Campos-Ortega, J.A., and Hartenstein, V. (1985). The embryonic development of Drosophila melanogaster (Berlin ; New York: Springer-Verlag).

Cavanaugh, K.E., Staddon, M.F., Munro, E., Banerjee, S., and Gardel, M.L. (2020). RhoA Mediates Epithelial Cell Shape Changes via Mechanosensitive Endocytosis. Dev Cell *52*, 152-166 e155.

Chen, P., Nordstrom, W., Gish, B., and Abrams, J.M. (1996). grim, a novel cell death gene in Drosophila. Genes & development *10*, 1773-1782.

Christley, S., Alber, M.S., and Newman, S.A. (2007). Patterns of mesenchymal condensation in a multiscale, discrete stochastic model. PLoS Comput Biol *3*, e76.

Clement, R., Dehapiot, B., Collinet, C., Lecuit, T., and Lenne, P.F. (2017). Viscoelastic Dissipation Stabilizes Cell Shape Changes during Tissue Morphogenesis. Curr Biol *27*, 3132-3142 e3134.

Dawi, M.A., and Munoz, J.J. (2021). Stability bounds of a delay visco-elastic rheological model with substrate friction. J Math Biol *83*, 71.

DeLise, A.M., Fischer, L., and Tuan, R.S. (2000). Cellular interactions and signaling in cartilage development. Osteoarthr Cartil *8*, 309-334.

Doubrovinski, K., Swan, M., Polyakov, O., and Wieschaus, E.F. (2017). Measurement of cortical elasticity in Drosophila melanogaster embryos using ferrofluids. Proc Natl Acad Sci U S A *114*, 1051-1056.

Erneux, T. (2009). Applied delay differential equations (New York: Springer).

Evans, I.R., Hu, N., Skaer, H., and Wood, W. (2010). Interdependence of macrophage migration and ventral nerve cord development in Drosophila embryos. Development *137*, 1625-1633.

Franze, K. (2013). The mechanical control of nervous system development. Development *140*, 3069-3077.

Franze, K., Janmey, P.A., and Guck, J. (2013). Mechanics in neuronal development and repair. Annu Rev Biomed Eng *15*, 227-251.

Frenz, D.A., Jaikaria, N.S., and Newman, S.A. (1989). The mechanism of precartilage mesenchymal condensation: a major role for interaction of the cell surface with the amino-terminal heparin-binding domain of fibronectin. Developmental biology *136*, 97-103.

Hall, B.K., and Miyake, T. (2000). All for one and one for all: condensations and the initiation of skeletal development. BioEssays *22*, 138-147.

226 Hartenstein, V., and Wodarz, A. (2013). Initial neurogenesis in Drosophila. Wiley
227 Interdiscip Rev Dev Biol *2*, 701-721.

228 Heisenberg, C.-P., and Bellaïche, Y. (2013). Forces in Tissue Morphogenesis and
229 Patterning. Cell *153*, 948-962.

230 Hogan, B.L. (1999). Morphogenesis. Cell *96*, 225-233.

231 Ito, K., Urban, J., and Technau, G.M. (1995). Distribution, classification, and
232 development ofDrosophila glial cells in the late embryonic and early larval ventral nerve
233 cord. Rouxs Arch Dev Biol *204*, 284-307.

234 Jorba, I., Uriarte, J.J., Campillo, N., Farre, R., and Navajas, D. (2017). Probing
235 Micromechanical Properties of the Extracellular Matrix of Soft Tissues by Atomic Force
236 Microscopy. J Cell Physiol *232*, 19-26.

237 Karkali, K., Saunders, T.E., Vernon, S.W., Baines, R.A., Panayotou, G., and Martín-
238 Blanco, E. (2020). JNK signaling in pioneer neurons directs the architectural organization
239 of the CNS and coordinates the motor activity of the Drosophila embryo. bioRxiv,
240 092486.

241 Khalilgharibi, N., Fouchard, J., Asadipour, N., Barrientos, R., Duda, M., Bonfanti, A.,
242 Yonis, A., Harris, A., Mosaffa, P., and Fujita, Y. (2019). Stress relaxation in epithelial
243 monolayers is controlled by the actomyosin cortex. Nat Physics *15*, 839-847.

244 Kiehart, D.P., and Feghali, R. (1986). Cytoplasmic myosin from Drosophila
245 melanogaster. J Cell Biol *103*, 1517-1525.

246 Kilinc, D. (2018). The Emerging Role of Mechanics in Synapse Formation and Plasticity.
247 Front Cell Neurosci *12*, 483.

248 Krzic, U., Gunther, S., Saunders, T.E., Streichan, S.J., and Hufnagel, L. (2012).
249 Multiview light-sheet microscope for rapid in toto imaging. Nat Methods *9*, 730-733.

250 Landgraf, M., Bossing, T., Technau, G.M., and Bate, M. (1997). The origin, location, and
251 projections of the embryonic abdominal motorneurons of Drosophila. J Neurosci *17*,
252 9642-9655.

253 Landgraf, M., Sanchez-Soriano, N., Technau, G.M., Urban, J., and Prokop, A. (2003).
254 Charting the Drosophila neuropile: a strategy for the standardised characterisation of
255 genetically amenable neurites. Dev Biol *260*, 207-225.

256 LeGoff, L., and Lecuit, T. (2015). Mechanical Forces and Growth in Animal Tissues.
257 Cold Spring Harb Perspect Biol *8*, a019232.

Li, Y., Muffat, J., Omer, A., Bosch, I., Lancaster, M.A., Sur, M., Gehrke, L., Knoblich, J.A., and Jaenisch, R. (2017). Induction of Expansion and Folding in Human Cerebral Organoids. Cell Stem Cell *20*, 385-396 e383.

Lin, D.M., Fetter, R.D., Kopczynski, C., Grenningloh, G., and Goodman, C.S. (1994). Genetic analysis of Fasciclin II in Drosophila: defasciculation, refasciculation, and altered fasciculation. Neuron *13*, 1055-1069.

Lynch, H.E., Crews, S.M., Rosenthal, B., Kim, E., Gish, R., Echiverri, K., and Hutson, M.S. (2013). Cellular mechanics of germ band retraction in Drosophila. Developmental biology *384*, 205-213.

Mammoto, T., and Ingber, D.E. (2010). Mechanical control of tissue and organ development. Development *137*, 1407-1420.

Martinek, N., Shahab, J., Saathoff, M., and Ringuette, M. (2008). Haemocyte-derived SPARC is required for collagen-IV-dependent stability of basal laminae in Drosophila embryos. J Cell Sci *121*, 1671-1680.

Matsubayashi, Y., Sanchez-Sanchez, B.J., Marcotti, S., Serna-Morales, E., Dragu, A., Diaz-de-la-Loza, M.D., Vizcay-Barrena, G., Fleck, R.A., and Stramer, B.M. (2020). Rapid Homeostatic Turnover of Embryonic ECM during Tissue Morphogenesis. Dev Cell *54*, 33-42 e39.

Mayer, M., Depken, M., Bois, J.S., Julicher, F., and Grill, S.W. (2010). Anisotropies in cortical tension reveal the physical basis of polarizing cortical flows. Nature *467*, 617-621.

Meyer, S., Schmidt, I., and Klambt, C. (2014). Glia ECM interactions are required to shape the Drosophila nervous system. Mech Dev *133*, 105-116.

Miller, C.J., and Davidson, L.A. (2013). The interplay between cell signalling and mechanics in developmental processes. Nat Rev Genet *14*, 733-744.

Mongera, A., Rowghanian, P., Gustafson, H.J., Shelton, E., Kealhofer, D.A., Carn, E.K., Serwane, F., Lucio, A.A., Giammona, J., and Campas, O. (2018). A fluid-to-solid jamming transition underlies vertebrate body axis elongation. Nature *561*, 401-405.

Muñoz, J.J., Dingle, M., and Wenzel, M. (2018). Mechanical oscillations in biological tissues as a result of delayed rest-length changes. Phys Rev E *98*, 052409.

Notbohm, J., Banerjee, S., Utuje, K.J.C., Gweon, B., Jang, H., Park, Y., Shin, J., Butler, J.P., Fredberg, J.J., and Marchetti, M.C. (2016). Cellular Contraction and Polarization Drive Collective Cellular Motion. Biophys J *110*, 2729-2738.

Oliveira, M.M., Shingleton, A.W., and Mirth, C.K. (2014). Coordination of wing and whole-body development at developmental milestones ensures robustness against environmental and physiological perturbations. PLoS Genet *10*, e1004408.

Olofsson, B., and Page, D.T. (2005). Condensation of the central nervous system in embryonic Drosophila is inhibited by blocking hemocyte migration or neural activity. Dev Biol *279*, 233-243.

Page, D.T., and Olofsson, B. (2008). Multiple roles for apoptosis facilitating condensation of the Drosophila ventral nerve cord. Genesis *46*, 61-68.

Pastor-Pareja, J.C., and Xu, T. (2011). Shaping cells and organs in Drosophila by opposing roles of fat body-secreted Collagen IV and perlecan. Dev Cell *21*, 245-256.

Petridou, N.I., and Heisenberg, C.P. (2019). Tissue rheology in embryonic organization. EMBO J *38*, e102497.

Petrolli, V., Le Goff, M., Tadrous, M., Martens, K., Allier, C., Mandula, O., Herve, L., Henkes, S., Sknepnek, R., Boudou, T.*, et al.* (2019). Confinement-Induced Transition between Wavelike Collective Cell Migration Modes. Phys Rev Lett *122*, 168101.

Peyret, G., Mueller, R., d'Alessandro, J., Begnaud, S., Marcq, P., Mege, R.M., Yeomans, J.M., Doostmohammadi, A., and Ladoux, B. (2019). Sustained Oscillations of Epithelial Cell Sheets. Biophys J *117*, 464-478.

Pipa, R.L. (1973). Proliferation, movement, and regression of neurons during the postembryonic development of insects. In Developmental Neurobiology of Arthropods (Cambridge: Cambridge University Press).

Redies, C., and Puelles, L. (2001). Modularity in vertebrate brain development and evolution. Bioessays *23*, 1100-1111.

Roig-Puiggros, S., Vigouroux, R.J., Beckman, D., Bocai, N.I., Chiou, B., Davimes, J., Gomez, G., Grassi, S., Hoque, A., Karikari, T.K.*, et al.* (2020). Construction and reconstruction of brain circuits: normal and pathological axon guidance. J Neurochem *153*, 10-32.

Sanchez-Soriano, N., Tear, G., Whitington, P., and Prokop, A. (2007). Drosophila as a genetic and cellular model for studies on axonal growth. Neural Dev *2*, 9.

Saunders, T.E., and Ingham, P.W. (2019). Open questions: how to get developmental biology into shape? BMC Biol *17*, 17.

Schindelin, J., Arganda-Carreras, I., Frise, E., Kaynig, V., Longair, M., Pietzsch, T., Preibisch, S., Rueden, C., Saalfeld, S., Schmid, B.*, et al.* (2012). Fiji: an open-source platform for biological-image analysis. Nat Methods *9*, 676-682.

Schulze, K.L., Broadie, K., Perin, M.S., and Bellen, H.J. (1995). Genetic and electrophysiological studies of Drosophila syntaxin-1A demonstrate its role in nonneuronal secretion and neurotransmission. Cell *80*, 311-320.

Schwabe, T., Li, X., and Gaul, U. (2017). Dynamic analysis of the mesenchymal-epithelial transition of blood-brain barrier forming glia in Drosophila. Biol Open *6*, 232-243.

Serwane, F., Mongera, A., Rowghanian, P., Kealhofer, D.A., Lucio, A.A., Hockenbery, Z.M., and Campas, O. (2017). In vivo quantification of spatially varying mechanical properties in developing tissues. Nat Methods *14*, 181-186.

Shellard, A., and Mayor, R. (2021). Collective durotaxis along a self-generated stiffness gradient in vivo. Nature *600*, 690-694.

Shklyar, B., Sellman, Y., Shklover, J., Mishnaevski, K., Levy-Adam, F., and Kurant, E. (2014). Developmental regulation of glial cell phagocytic function during Drosophila embryogenesis. Developmental biology *393*, 255-269.

Shyer, A.E., Rodrigues, A.R., Schroeder, G.G., Kassianidou, E., Kumar, S., and Harland, R.M. (2017). Emergent cellular self-organization and mechanosensation initiate follicle pattern in the avian skin. Science *357*, 811-815.

Singh, P., and Schwarzbauer, J.E. (2012). Fibronectin and stem cell differentiation - lessons from chondrogenesis. J Cell Sci *125*, 3703-3712.

Solon, J., Kaya-Copur, A., Colombelli, J., and Brunner, D. (2009). Pulsed forces timed by a ratchet-like mechanism drive directed tissue movement during dorsal closure. Cell *137*, 1331-1342.

Spedden, E., and Staii, C. (2013). Neuron biomechanics probed by atomic force microscopy. Int J Mol Sci *14*, 16124-16140.

Staddon, M.F., Cavanaugh, K.E., Munro, E.M., Gardel, M.L., and Banerjee, S. (2019). Mechanosensitive Junction Remodeling Promotes Robust Epithelial Morphogenesis. Biophys J *117*, 1739-1750.

Stark, M.R., Sechrist, J., Bronner-Fraser, M., and Marcelle, C. (1997). Neural tube-ectoderm interactions are required for trigeminal placode formation. Development *124*, 4287-4295.

Stépán, G. (1989). Retarded dynamical systems : stability and characteristic functions (Harlow: Longman Scientific and Technical).

Sumi, A., Hayes, P., D'Angelo, A., Colombelli, J., Salbreux, G., Dierkes, K., and Solon, J. (2018). Adherens Junction Length during Tissue Contraction Is Controlled by the Mechanosensitive Activity of Actomyosin and Junctional Recycling. Dev Cell *47*, 453-463 e453.

Swanson, L.W. (2007). Quest for the basic plan of nervous system circuitry. Brain Res Rev *55*, 356-372.

Technau, G.M. (2008). Brain development in Drosophila melanogaster, Vol 628 (Springer Science+Business Media, LLC - Landes Bioscience).

Tessier-Lavigne, M., and Goodman, C.S. (1996). The molecular biology of axon guidance. Science *274*, 1123-1133.

Thielicke, W., and Stamhuis, E.J. (2018). The effects of wing twist in slow-speed flapping flight of birds: trading brute force against efficiency. Bioinspir Biomim *13*, 056015.

Tiwari, P., Rengarajan, H., and Saunders, T.E. (2021). Scaling of internal organs during Drosophila embryonic development. Biophys J *120*, 4264-4276.

Vig, D.K., Hamby, A.E., and Wolgemuth, C.W. (2016). On the Quantification of Cellular Velocity Fields. Biophys J *110*, 1469-1475.

Weber, G.F., Bjerke, M.A., and DeSimone, D.W. (2011). Integrins and cadherins join forces to form adhesive networks. J Cell Sci *124*, 1183-1193.

Zhang, H., and Labouesse, M. (2012). Signalling through mechanical inputs: a coordinated process. J Cell Sci *125*, 3039-3049.

Zlatic, M., Li, F., Strigini, M., Grueber, W., and Bate, M. (2009). Positional cues in the Drosophila nerve cord: semaphorins pattern the dorso-ventral axis. PLoS Biol *7*, e1000135.

SUPPLEMENTARY FIGURES LEGENDS

Figure S1

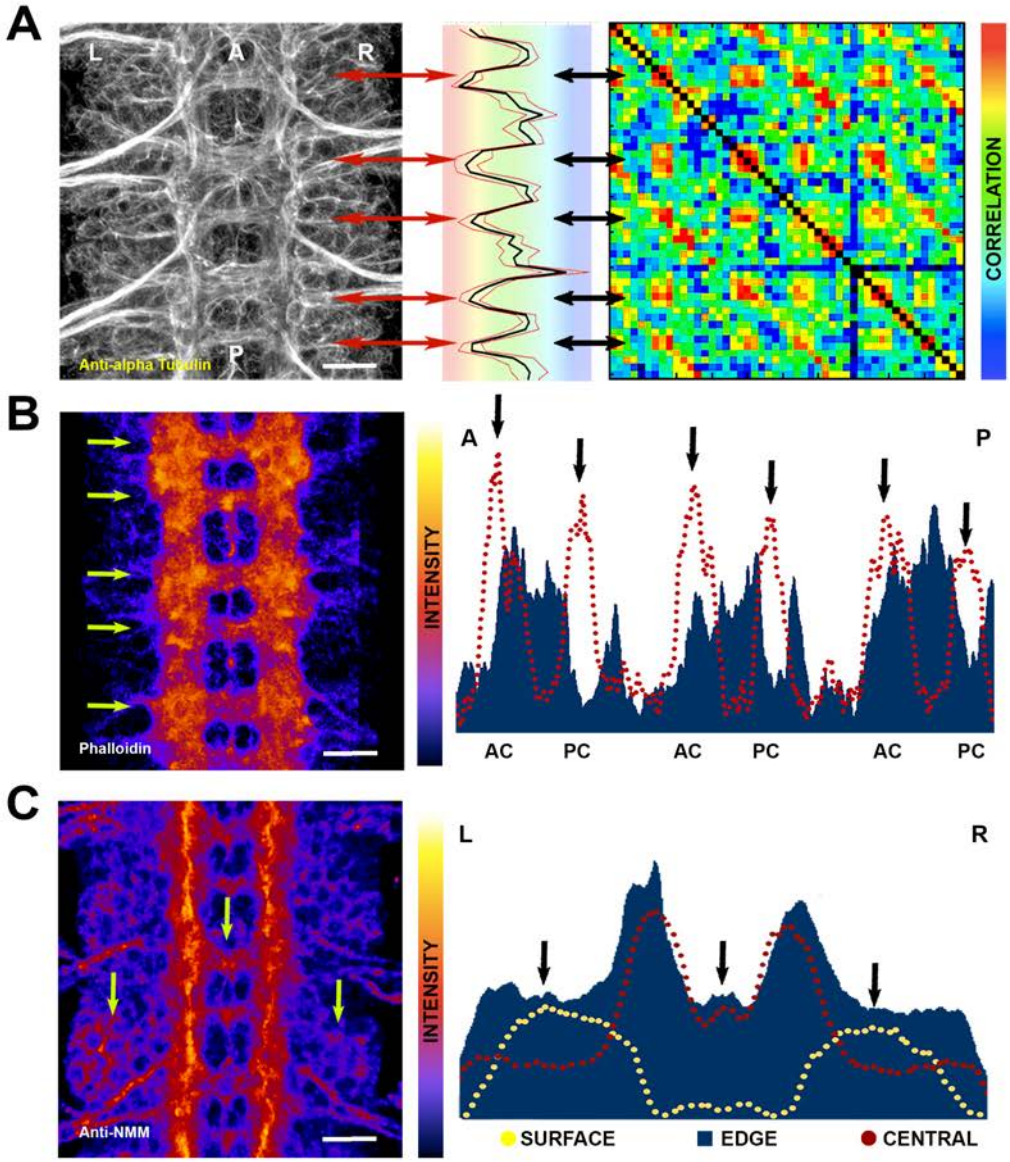

Figure S1: VNC Cytoskeleton structural organization

A) Acetylated α-Tubulin immunoreactivity. Left; maximum projection of a ventral view of three abdominal segments (A2 to A4) of the VNC of a 16-stage embryo. Left (L) and Right (R) and Anterior (A) and Posterior (P) orientation are labelled. Scale Bar is 10 µm. Middle; image cross-correlation score [mean (black) and ± standard deviation (red)] along the AP axis. Right; self cross-correlation matrix of the Z sections of the same image.

The color-coded representation shows the correlation level (red-maximum to blue-minimum) for each possible cross comparison at each position of the image divided in 50 bins (see Experimental Procedures). Two axonal nodes with robust maximum correlation are conserved from segment to segment. **B)** Phalloidin (Actin) distribution. Left; maximum projection of a ventral view of three abdominal segments (A2 to A4) of the VNC of a 16-stage embryo. Signal Intensity is color coded (Fire LUT). Arrows point to the anterior and posterior commissures. Scale Bar is 10 µm. Right; Actin intensity profile along the AP axis: Discontinued Red at the ventral midline highlighting the anterior (AC) and posterior commissures (PC) (arrows). Solid Blue at the main contralateral trunks uncovering a stereotyped segmentally iterated distribution. **C)** Non-Muscle Myosin (NMM - Myosin II) imunoreactivity. Left; maximum projection of a ventral view of three abdominal segments (A2 to A4) of the VNC of a 16-stage embryo. Signal Intensity is color coded (Fire LUT). Arrows point to the lateral (left and right) and central neuropile domains. Scale Bar is 10 µm. Right; NMM intensity profile transversal to the AP axis: Discontinued Yellow at the ventral surface of the VNC highlighting the NMM accumulation at the lateral domains around the neurons cell bodies; Solid Blue at the medial edge of the longitudinal axonal trunks showing the preferential acumulation of NMM at contralateral single-cell domains at the dorsomedial edge; and Discontinued Red at the middle of the VNC trunk. See also **Movie S1**.

Figure S2

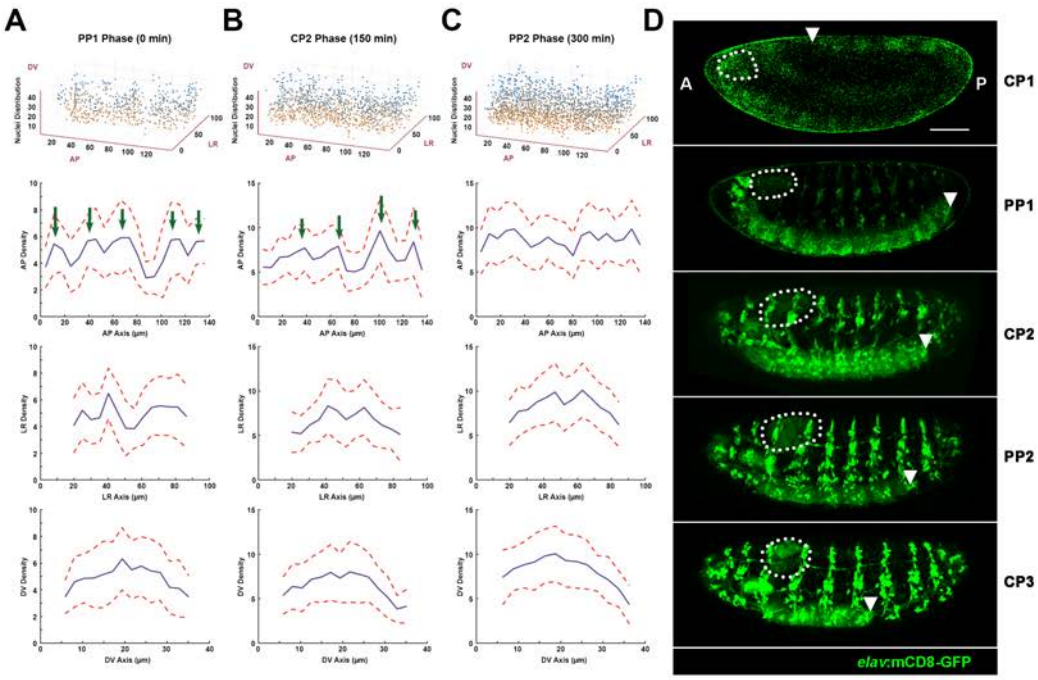

409

410 **Figure S2: VNC condensation temporal development and spatial distribution of cell**
411 **density**

412 Density of neurons cell bodies along condensation progression: **A)** PP1 phase; **B)** CP2
413 phase; **C)** PP2 phase. Top row: 3D representation of the spatial position of the neurons
414 cell nucleus at the respective time points, with color coding representing height along the
415 DV-axis. Second row: Average number of nuclei neighbouring each nucleus (AP density)
416 along the AP axis. Third row: Average number of nuclei neighbouring each nucleus along
417 the left-right (LR) axis. Fourth row: Average number of nuclei neighbouring each nucleus
418 along the DV axis. In all panels the blue curve is mean and the dashed red line represent
419 ±1 s.d. Green arrows denote peaks in the density. D) Snapshots corresponding to the five
420 phases of VNC condensation (CP1, PP1, CP2, PP2, CP3) from a time lapse (Movie S2)

of an Elav-Gal4>UAS-mCD8-GFP embryo (lateral view) recorded by confocal microscopy. mCD8-GFP labelling marks all neural derivatives. Dotted shapes indicate the position of the brain lobes. Arrowheads denote the posterior tip of the VNC. AP axis orientation is indicated. Scale bar 50µm. We calculated the nuclei density by quantifying the number of nuclei that were within a sphere of radius 7.5mm from each nucleus. We did not calculate the density for nuclei near the tissue edges to minimize boundary effects.

Figure S3

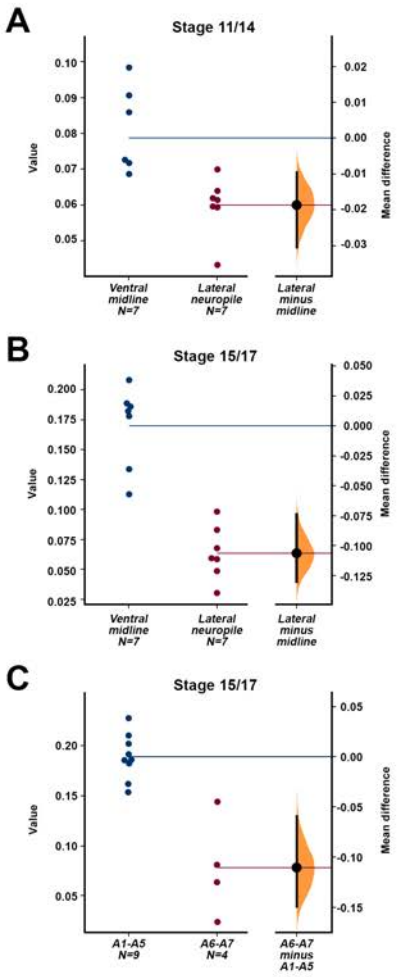

Figure S3: Quantification of VNC material properties during condensation

A) Statistical analysis of measured E (stiffness values) at different positions from stage 11-14 (estimationstats.com). Data points are shown on the left. The confidence interval is shown on right. $p < 0.05$ from Mann-Witney test. **B)** As **(A)**, but for late stages 15-17. $p < 10\text{-}2$ from Mann-Witney test. **C)** As **(B)**, but comparing the E measured in anterior domains (A1-A5) with those of posterior domains (A6-A7). $p < 10\text{-}2$ from Mann-Witney test.

Figure S4

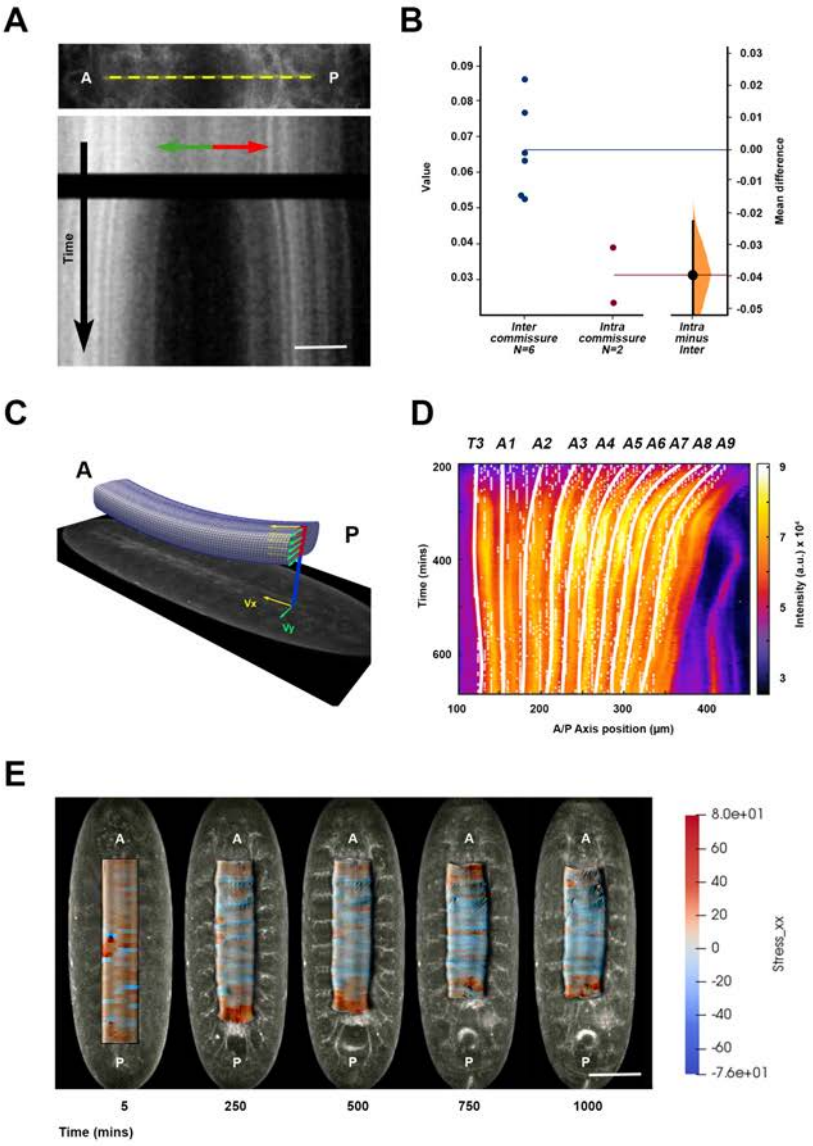

Figure S4: Analyses of laser microsurgery of the VNC and details of the finite elements model

A) (Top) VNC tissue recoil after generating a laser cut perpendicular to the AP axis of a stage 14 embryo expressing alpha Tubulin-GFP. Yellow dashed line indicates the region of analysis. (Bottom) Kymograph of VNC recoil after laser ablation. Green (anterior) and red (posterior) arrows indicate tissue recoil directionality. The black transversal domain spans the period of laser cutting. Scale bar 10 µm. **B)** Analysis of VNC recoil speed, at

inter- and intracommissural domains. Confidence interval on right. Generated using estimationstats.com. **C)** Mapping of the measured velocities from PIV onto the FE model. Each velocity on the (x, y) plane is mapped onto points of the deformed mesh with closer (x, y) positions. Nodes with non-associated velocity were deformed according to Cauchy's equilibrium equation for a viscoelastic material and discretized (see Experimental Procedures). **D)** As **Figure 3F**, but showing the points of maximum compression (minimum value of $\sigma^{""}$) before (white dots) and after smoothing (white lines). **E)** Snapshots of deformed FE model showing contour plot of the AP normal stress $\boldsymbol{\sigma_{xx}}$ superimposed over the corresponding images (ventral view) of Fas2-GFP embryos. Scale bar 50 μm.

Figure S5

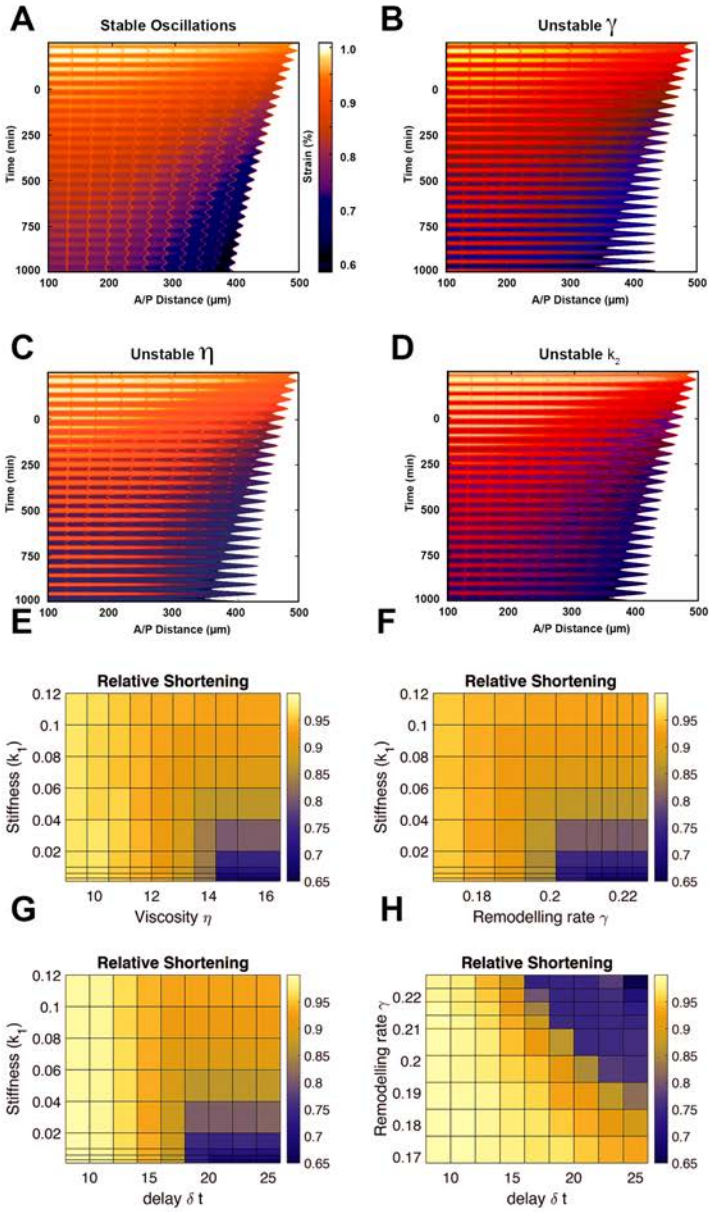

Figure S5: Kymographs of rest-length and condensation diagrams on four planes of the parameter space

A-D) Rheological model with delay using different material parameters and numerical simulation **A)** Stable oscillation using reference values: remodeling rate $\gamma = 0.21\ s^{-1}$, viscous friction $\eta = 15$ Pa.s., delay $\Delta t = 20$ s, and stiffnesses $k_1 = 0.01$ Pa and $k_2 = 1.9$ Pa, respectively. Initial rest-length is $L_0 = 0.95 l_0$, with l_0 being the initial apparent length. **B)**

Unstable oscillations due to increase of remodeling rate ($\gamma = 0.22\ s^{-1}$). **C)** Unstable oscillations due to increase of viscosity η=16 Pa.s. **D**) Unstable oscillations due to decrease of stiffness k_2 =1.8 Pa. **E-H)** Relative shortening measured as the relative final length, l_{final}/l_0, for different combinations of perturbed values of model parameters: elastic stiffness k_1, viscosity η, delay δt, and remodeling rate γ. **A)** Stifness / Viscosity. **B)** Stifness / Remodeling rate. **C)** Stifness / Delay time. **D)** Remodeling rate / Delay time. Values have been chosen around the reference parameters (k_1, η, δt, γ) = (0.01, 15, 20, 0.2). Effects of stiffness κ_2 of viscoelastic branch are similar to those of k_1.

Figure S6

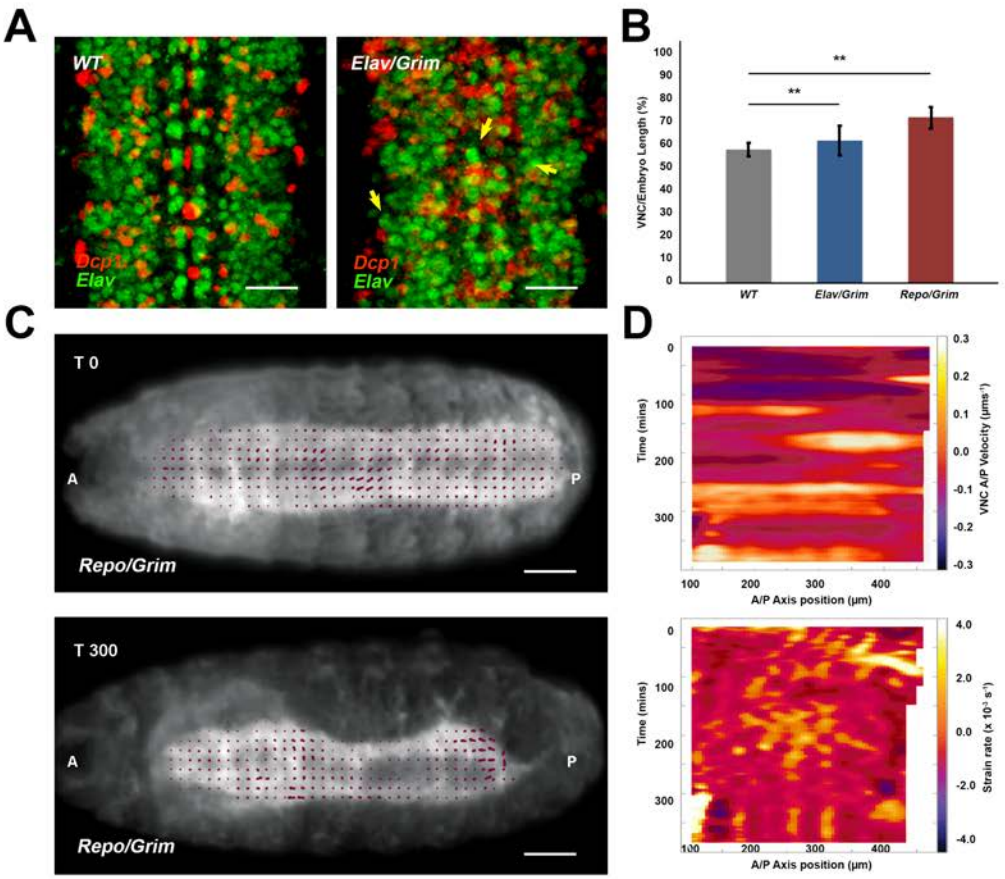

Figure S6: Large-scale forces and local tissue dynamics are modulated by neurons and glia

A) CNS Flat-preps of WT (top) and Elav-Gal4>UAS-Grim (bottom) embryos, at stage 16, immunostained for Dcp1 (red) and Elav (green). Yellow arrowheads point to ELAV positive, Dcp1 negative cells, which are neurons that have not engaged to apoptosis. Scale bar 10 µm. **B)** Quantification of VNC length (VNC/Embryo Length %) of WT (gray), Elav-Gal4>UAS-Grim (blue) and Repo-Gal4>UAS-Grim (red) embryos, at stage 16. Bars represent mean values (n=6 embryos). **$p < 10^{-2}$. **C)** Snapshots from light-sheet

imaging recordings of a Repo-Gal4::UAS-mCD8-GFP::His2Av-mRFP>UAS-Grim embryo (ventral view) at two different times of development (Stages 15-17) **(Movie S10)**. Magenta arrows denote local velocity trajectories from PIV analyses. AP axis orientation is indicated. Scale bar 50 µm. **D)** Velocity (as in **Figure 1C**) and strain rate (as in **Figure 2D**) kymographs for a representative Repo-Gal4>UAS-Grim embryo. No periodic oscillations were observed.

Figure S7

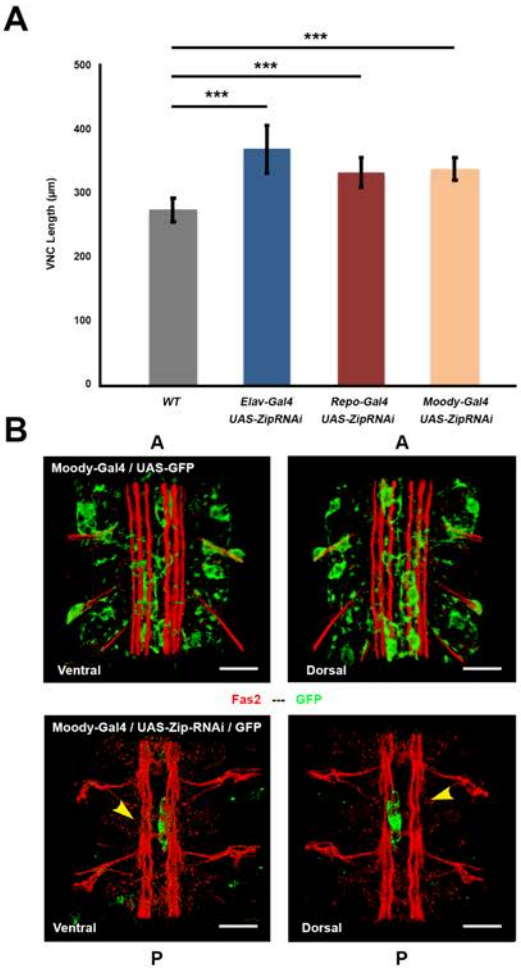

494

495 **Figure S7: Subperineural glia contractility is necessary for condensation and VNC**

496 **organization.**

497 **A)** Quantification of VNC length of WT (gray), Elav-Gal4>UAS-Zip-RNAi (blue),
498 Repo-Gal4>UAS-Zip-RNAi (red) and Moody-Gal4>UAS-Zip-RNAi embryos (orange),
499 at stage 16. Bars represent mean values (n = 5 embryos). ***p < 10-3. **B)** Ventral and
500 Dorsal 3D views of dissected, stage 16, control (top) and Moody-Gal4::UAS-mCD8-
501 GFP>UAS-Zip-RNAi (bottom) embryos, immunostained for Fas2 (red) and GFP (green).
502 Yellow arrowheads point to the disrupted axonal network. AP axis orientation is
503 indicated. Scale bar 10 µm.

SUPPLEMENTARY MOVIES LEGENDS

Movie S1. VNC Cytoskeleton structural organization

Animated 3D reconstruction of a section of the VNC of a late *Drosophila* embryo (Stage 16) highlighting the levels of expression (Fire Lut) of different cytoskeletal components: the axonal pattern stained with anti Acetylated α-Tubulin antibodies (left); the iterated segmental distribution of actin (Phalloidin staining) along the AP axis (centre); and the distribution of NMM accumulating at the longitudinal dorsomedial edges of the neuropile. Scale bar 15 µm.

Movie S2. Dynamics of VNC condensation

Time lapse of an elav-Gal4>UASmCD8-GFP embryo (lateral view) recorded by confocal microscopy. mCD8-GFP labeling marks all neural derivatives. AP axis orientation is indicated. Time in hours. Scale bar 50 µm.

Movie S3. Isotropic three-dimensional reconstructions of embryo images

Time lapse recorded by multi-view light-sheet imaging of a live Histone2Av-mCherry embryo (ventral view). mCherry labeling marks all nuclei and was used to correct the embryo twitching. Raw data is shown on the top and "detwitched" images on the bottom. AP axis orientation is indicated. Time in hours. Scale bar 50µm.

Movie S4. Anterior and posterior contractile oscillations (stationary domain)

Time Lapse recording of an embryo expressing Fas2-GFP (Top - ventral view; Bottom - re-slice over the Z-axis) acquired by Confocal Microscopy. The double headed arrow points to the stationary domain where converge anterior and posterior condensation. AP axis orientation is indicated. Time in hours. Scale bar 50µm.

Movie S5. VNC response to laser microsurgery during condensation

Laser ablation of stage 14 embryos expressing alpha Tubulin-GFP. The recoil of intercommissural (left) and intracommissural (right) cuts are compared. Yellow lines highlight the position of the laser cuts. AP axis orientation is indicated. Time in seconds. Scale bar 20μm.

Movie S6. VNC condensation is segmentally autonomous

Evolution over time of a laser cut at the intercommissural space between the abdominal segments A1 and A2, of a stage 14 embryo, expressing alpha Tubulin-GFP. After ablation, the individual neuromeres (color coded dots at the bottom mark the positions of the anterior and posterior commissures of each neuromere at sequential times) continue to condense autonomously. Yellow line highlights the position of the laser cut. AP axis orientation is indicated. Time in hours. Scale bar 20μm.

Movie S7. Three-dimensional Finite Element model (FE)

The measured velocity field was mapped onto the FE model to reconstruct strain and stress fields. Evolution through time of contour plots of AP stresses σ'''' (FE model) superimposed over experimental live images (ventral view) of an embryo expressing Fas2-GFP. AP axis orientation is indicated. Time in hours. Scale bar 50μm.

Movie S8. Glia participates in the architectural organization of the VNC and its condensation

Time lapse recordings of WT (Top) and Repo-Gal4>UAS-Grim (bottom) embryos in an alpha Tubulin-GFP background (ventral view) acquired by Confocal Microscopy. AP axis orientation is indicated. Time in hours. Scale bar 50μm.

Movie S9. VNC condensation requires the mechanical contribution of glia

Light-sheet imaging record of a Repo-Gal4::UAS-mCD8-GFP::His2Av-mRFP>UAS-Grim embryo (ventral view) at different times of development (Stages 15-17). Magenta

arrows denote local velocity trajectories from PIV analyses. The VNC is significantly elongated and misshaped. AP axis orientation is indicated. Time in hours. Scale bar 50 μm.

Movie S10. Distinct roles for neurons and glia in VNC architecture and condensation

Time lapse recordings of embryos expressing Fas2-GFP, monitored by confocal imaging. From top to bottom, condensation dynamics in control (WT); Elav-Gal4>UAS-Zip-RNAi and Repo-Gal4>UAS-Zip-RNAi embryos. AP axis orientation is indicated. Time in hours. Scale bar 50 μm.

Movie S11. Finite Element model of VNC condensation

Three-dimensional representation of VNC condensation. FE model showing the evolution through time of contour plots of AP displacements (top) and experimental live images (ventral view) of an embryo expressing Fas2-GFP (bottom). AP axis orientation is indicated. Time in hours.

Movie S12. Myosin-mediated contractility in neurons and glia is required for VNC condensation

Finite element simulations with mapped velocities of control (WT); Elav-Gal4>UAS-Zip-RNAi and Repo-Gal4>UAS-Zip-RNAi embryos. Contour plots in the top row show the AP displacement fields and in the bottom row the elastic strains ε_{xx}.